POEM: A Fast Defocus Estimation Method for Scanning Transmission Electron Microscopy

Arturo Tejada
Delft Center for Systems and Control
Delft University of Technology
Mekelweg 2, 2628CD, Delft, The Netherlands

Arnold J. den Dekker
Delft Center for Systems and Control
Delft University of Technology
Mekelweg 2, 2628CD, Delft, The Netherlands

***Abstract*—The defocus polar rose estimation method (POEM) is introduced here as an alternative method for defocus estimation in scanning transmission electron microscopy. Its principle of operation is discussed in detail along with the results of initial simulation-based performance tests. The results show that POEM can attain a precision similar to that of equivalent methods in the literature but using significantly less data, thus increasing the defocus estimation speed significantly.**

I. Introduction

Scanning transmission electron microscopes (STEMs) are the tools of choice for academic research in material sciences, nanotechnology, and biology. They are also highly valued in, among others, the semiconductor industry, where they are used for production monitoring, control and troubleshooting. In both the academic and industrial sectors, STEMs are increasingly used to perform routine and repetitive measurements at the nano-scale (e.g., measuring nano-particles). Currently, performing such measurements is a labor-intensive task that involves time-consuming steps such as microscope calibration. Thus, there is an unequivocal need for a new generation of STEMs capable of performing nano-measurements autonomously and with high-speed.

Automating microscope calibration, therefore, is needed to attain this goal. It involves correcting the microscope's optical properties to ensure a certain level of image 'quality'. In a STEM, the main optical properties are spherical aberration, astigmatism, and defocus. Since these properties can only be observed from image data, their manual calibration requires the STEM operators to repeatedly acquire and visually interpret images and to adjust the STEM controls accordingly. Although many methods have been proposed to automate microscope calibration (see, e.g., [1], [2] and the references therein), they rely on estimating the optical properties automatically from one or more STEM images, which are acquired relatively slowly (see below). Thus, to enable high-speed automation faster estimation methods are needed.

The defocus Polar rOse Estimation Method (POEM) is introduced here as a fast alternative for defocus estimation. As it is shown in the sequel through a set of simulation-based performance tests, POEM requires significantly less image data (up to 50 times less) and data processing time than the standard defocus estimation methods. Since defocus calibration must be performed often, these tests suggest that POEM can have a large impact in STEM high-speed automation, specially if it is part of a defocus control scheme (see [2], [3]). The rest of the paper is organized as follows: Section II presents the STEM principle of operation, discusses the modeling of bright-field images, and describes some standard defocus estimation methods. Section III introduces the defocus POEM, along the results of the initial performance tests. Finally, our conclusions are given in Section IV.

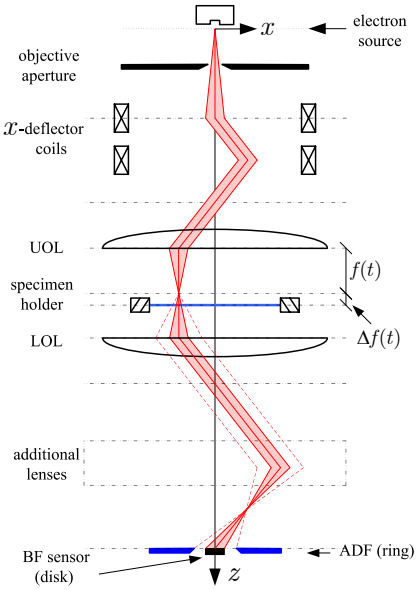

Fig. 1. Main STEM components. The ray diagram illustrates the bright-field image formation process.

II. STEM Operation and Defocus Estimation

This section contains two parts. The firt part describes the STEM principle of operation and motivates the need for measuring the defocus. The second part describes the a particular STEM image type, brigh-field images, and the standard defocus estimation procedures based on them.

A. Principle of Operation

As Figure 1 shows, STEMs operate under a principle similar to that of analog oscilloscopes [4]: An electron source, generates an electron beam that is demagnified by the upper part of an objective lens (UOL) into a small probe at a specimen. The electrons that go through the specimen are

978-1-4244-7934-4/11/$26.00 ©2011 IEEE

scattered at different angles depending on the atomic weight of the atoms under the probe. Those that are scattered at small angles are 'counted' by a small disc-shaped sensor, while those that are scattered at high angles are collected and counted by a ring sensor, (these are, respectively, the bright-field (BF) and the annular dark-file (ADF) sensors in Figure 1). Note that the electrons are 're-centered' to the optical axis (z-axis in Figure 1) by the lower part of the objective lens (LOL) before they hit the sensors. The latter generate signals with amplitude proportional to the number of detected electrons. Images are then created by sweeping the probe over the specimen in a raster pattern, by means of deflector coils, and plotting the amplitude of sensor signals as functions of the probe's position. Depending on the (sensor) signal, this procedure leads to either bright-field images or to annular dark-field images.

It is clear from this description that the image quality is determined by probe's characteristics, which are in turn set by the objective lens optical properties [5]. In essence, this lens is a round coil, whose current-controlled magnetic field focuses the electrons at a focal distance, f below the lens (see Figure 1). If the electrons are not focused on the surface of the specimen the images become blurred. This error in the focusing distance is called defocus and is denoted Δf. The objective lens also presents spherical aberration and astigmatism. Due to the former, electrons with a trajectory that lies closer to the optical axis are focused less strongly than those with trajectories that lie farther from the axis. Due to astigmatism, electrons with different trajectory angles (measured in the $x-y$ plane with respect to the $x-$axis) tend to be focused at different focal distances, thus given the probe an elliptical (instead of circular) shape. Note that although all three effects degrade the direct image interpretation (by blurring and deforming the images), they can also contribute to maximize the precision of image-based measurements [6], [7], which motivates the need for both measuring and controlling them. In the sequel, however, the attention will be restricted to the defocus, and it will be assumed that the objective lens is astigmatism-free and has a constant spherical aberration (which is the case in practice). As explained below, the defocus POEM uses bright-field image data. The modeling of such images is explained next.

B. Bright-Field Images and Standard Defocus Estimation

Defocus is often estimated from bright-field images of thin amorphous specimens. For a fixed defocus, these images are modeled by random functions, $\boldsymbol{I} : \mathbb{R}^2 \to \mathbb{R}$, given by [8]

$$\boldsymbol{I}(x, y) = 1 + 2\sigma(\boldsymbol{v} * p)(x, y).^1 \tag{1}$$

Here, σ is the interaction constant; $\boldsymbol{v}$, a zero-mean white noise process with variance ς^2, models the specimen's projected potential function [5]; $*$ denotes convolution; and $p \triangleq \mathfrak{F}^{-1}\{P\}$, is the objective lens point spread function, with transfer function $P : \mathbb{R}^2 \to \mathbb{R}$ ($\mathfrak{F}$ denotes the Fourier transform). In the absence of astigmatism, P (and, hence, p [9]) is circular symmetric with radial profile, $\mathfrak{P} : \mathbb{R}^+ \to \mathbb{R}$, given by

$$\mathfrak{P}(q) = A(q)\sin(\chi(q))E(q). \tag{2}$$

In (2), $A : \mathbb{R}^+ \to \mathbb{R}$ models the effect of the objective aperture ($A(q) = 1$ for $q < q_a$ and 0 otherwise). $\chi : \mathbb{R}^+ \to \mathbb{R}$, the aberration function, describes the objective lens deviation from an ideal lens in the frequency domain. It is given by [5]

$$\chi(q) = \pi(0.5C_s\lambda^3 q^4 - \Delta f \lambda q^2), \tag{3}$$

where λ is the electrons' wavelength and $C_s > 0$ and Δf denote the strength of, respectively, the lens' spherical aberration and defocus. Finally, the envelope function, $E : \mathbb{R} \to \mathbb{R}$, models the deviation of the electron source from an ideal one. It is given by

$$E(q) = \exp\left(-\frac{\pi^2\lambda^2\delta^2 q^4}{16\log(2)} - \pi^2 q_o^2[C_s\lambda^3 q^3 - \Delta\lambda q]^2\right), \tag{4}$$

where δ and q_o parameterize the electrons' energy spread and the electron source width, respectively [5].

Note that the zeros of $\mathfrak{P}$, for $q < q_a$, coincide with those of $\sin(\chi(\cdot))$. These, in turn, are uniquely determined by the values of C_s and Δf. This observation led to the standard (Thon ring) defocus estimation approach [2], [10], [11]:

1) Compute the modulus squared of the Fourier transform of a bright field image from a thin amorphous specimen.
2) Through radial averaging, estimate the radial profile of the resulting image. For $q > 0$, the estimated profile is proportional to $\mathfrak{P}^2$ [2].
3) Find the position of the local minima in the estimated profile (i.e., the position of the zeros in $\mathfrak{P}$), and from these estimate Δf (and C_s if it is unknown).

The speed of this procedure is limited mainly by step 1. For instance, it takes about 5.2 s to acquire a 512×512 pixels STEM bright field image, when using a typical pixel-dwell time of 20 μs. A second speed limiting factor is the data interpolation that is needed to compute the radial average (since images are always acquired using a rectangular scan pattern). Both factors are improved upon by the new defocus POEM which, as is explained next, makes use of only a few radial image lines and avoids data interpolation completely.

III. The Defocus POEM

This method estimates the defocus directly from real-space data. As is explained next, the autocorrelation of every image line that crosses the microscope's optical axis coincides with the inverse Hankel transform of $\mathfrak{P}^2$. The mathematical details are given in Subsection A, together with the main POEM steps. Subsection B discusses a particular POEM implementation and the result of initial simulation studies.

[1] Boldface characters denote random objects and processes. The latter, their stationarity and their ergodicity are defined over space, not over time.

$$
\begin{aligned}
&\mathbf{E}\{\boldsymbol{I}_\theta(\tau)\boldsymbol{I}_\theta(\tau+r)\} \\
&\quad= \mathbf{E}\left\{\int_{-\infty}^{+\infty}\int_{-\infty}^{+\infty}\boldsymbol{v}(x,y)p(\tau\cos\theta-x,\tau\sin\theta-y)dxdy\int_{-\infty}^{+\infty}\int_{-\infty}^{+\infty}\boldsymbol{v}(\tilde{x},\tilde{y})p((\tau+r)\cos\theta-\tilde{x},(\tau+r)\sin\theta-\tilde{y})d\tilde{x}d\tilde{y}\right\} \\
&\quad= \int_{-\infty}^{+\infty}\int_{-\infty}^{+\infty}\int_{-\infty}^{+\infty}\int_{-\infty}^{+\infty}\mathbf{E}\{\boldsymbol{v}(x,y)\boldsymbol{v}(\tilde{x},\tilde{y})\}p(\tau\cos\theta-x,\tau\sin\theta-y)p((\tau+r)\cos\theta-\tilde{x},(\tau+r)\sin\theta-\tilde{y})dxdyd\tilde{x}d\tilde{y} \\
&\quad= \int_{-\infty}^{+\infty}\int_{-\infty}^{+\infty}\left(\int_{-\infty}^{+\infty}\int_{-\infty}^{+\infty}\varsigma\delta(x-\tilde{x},y-\tilde{y})p(\tau\cos\theta-x,\tau\sin\theta-y)dxdy\right)p((\tau+r)\cos\theta-\tilde{x},(\tau+r)\sin\theta-\tilde{y})d\tilde{x}d\tilde{y} \\
&\quad= \int_{-\infty}^{+\infty}\int_{-\infty}^{+\infty}p(\tau\cos\theta-\tilde{x},\tau\sin\theta-\tilde{y})p(r\cos\theta-(\tilde{x}-\tau\cos\theta),r\sin\theta-(\tilde{y}-\tau\sin\theta))d\tilde{x}d\tilde{y} \qquad (6)
\end{aligned}
$$

A. POEM Foundation: Radial Image Line Autocorrelation

For a fixed $\theta \in [0, 2\pi)$, let $\boldsymbol{I}_\theta : \mathbb{R}^+ \to \mathbb{R}$ denote the radial image line given by

$$
\begin{aligned}
\boldsymbol{I}_\theta(r) &\triangleq \frac{\boldsymbol{I}(r\cos\theta, r\sin\theta) - 1}{2\sigma} \\
&= \int_{-\infty}^{+\infty}\int_{-\infty}^{+\infty}\boldsymbol{v}(x,y)p(r\cos\theta-x, r\sin\theta-y)dxdy. \qquad (5)
\end{aligned}
$$

Next, let $\mathcal{R}_\theta : \mathbb{R}^2 \to \mathbb{R}$ denote the line autocorrelation. That is, $\mathcal{R}_\theta(\tau, r) = \mathbf{E}\{\boldsymbol{I}_\theta(\tau)\boldsymbol{I}_\theta(\tau+r)\}$, $(\tau, r) \in \mathbb{R}^2$ ($\mathbf{E}\{\cdot\}$ is the expected value operator). Thus, (6) (see above) implies, after the change of variables $(x, y) = (\tilde{x} - \tau\cos\theta, \tilde{y} - \tau\sin\theta)$, that

$$
\mathcal{R}_\theta(\tau, r) = \int_{-\infty}^{+\infty}\int_{-\infty}^{+\infty}p(-x,-y)p(r\cos\theta-x, r\sin\theta-y)dxdy.
$$

Note that the integral above is $(p * p)(r\cos\theta, r\sin\theta)$ (since p is even). Also note that $\mathfrak{F}\{p * p\} = P^2$, so $p * p$ is circular symmetric. Thus, $\mathcal{R}_\theta$ is independent of τ and θ. Moreover, if $\mathfrak{p}$ is the radial profile of $p * p$, it follows that

$$
\mathcal{R}_\theta(\tau, \cdot) = \mathfrak{p} = \mathfrak{H}^{-1}\{\mathfrak{P}^2\}, \qquad (6)
$$

where $\mathfrak{H}^{-1}$ denotes the inverse, zero-order Hankel transform [9]. Note from (3) and (4) that $\mathfrak{P}$ is completely characterized by C_s, δ, q_o, and Δf. Since, in general, C_s, δ, and q_o are fixed and known beforehand, it follows from (6) that a defocus estimate, $\Delta\hat{f}$, can be found as follows:

$$
\Delta\hat{f} = \arg\min_{\Delta f}\|\hat{\mathfrak{p}} - \mathfrak{H}^{-1}\{\mathfrak{P}^2_{\Delta f}\}\|^2, \qquad (7)
$$

where $\hat{\mathfrak{p}}$ is the line autocorrelation estimated from one or more experimental radial image lines, and $\mathfrak{P}_{\Delta f}$ denotes the fact that $\mathfrak{P}$, $0 \le q \le q_a$, is parameterized by Δf. This provides the foundation for the defocus POEM, which can be summarized as follows:

1) Acquire several radial image lines, using the "polar rose" scan pattern depicted in Figure 2.

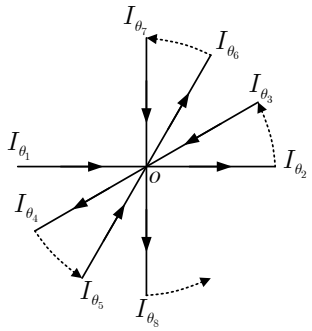

Fig. 2. Polar rose scan pattern for the defocus POEM. Eight radial image lines are shown. O denotes the optical axis.

2) Calculate $\hat{\mathfrak{p}}$ by averaging the estimated autocorrelation function of each acquired radial image line.
3) Estimate the defocus by solving the minimization problem (7).

There are several possible implementations of this procedure. One of them is discussed next, together with the results of initial simulation studies.

B. POEM Implementation and Simulation Studies

The main challenges in implementing the defocus POEM procedure are the estimation of the image line autocorrelations and the computation of (7). These are discussed next. They are followed by the details of our simulation studies.

Line Autocorrelation Estimation: Note from (1), (5), and (6) that $\boldsymbol{I}_\theta$ is a zero-mean, stationary stochastic process. Thus, its autocorrelation can be estimated using the standard, non-parametric estimators (see, e.g., [12]). Alternatively, under the further mild assumption that $\boldsymbol{I}_\theta$ has a rational spectral density (i.e., that the spectral density can be expressed as the ratio of two polynomials over q), $\boldsymbol{I}_\theta$ can be considered to be the output of a linear system driven by white noise [13] and, consequently, its autocorrelation can be estimated using parametric estimators, such as ARMASA [14], [15]. (In the

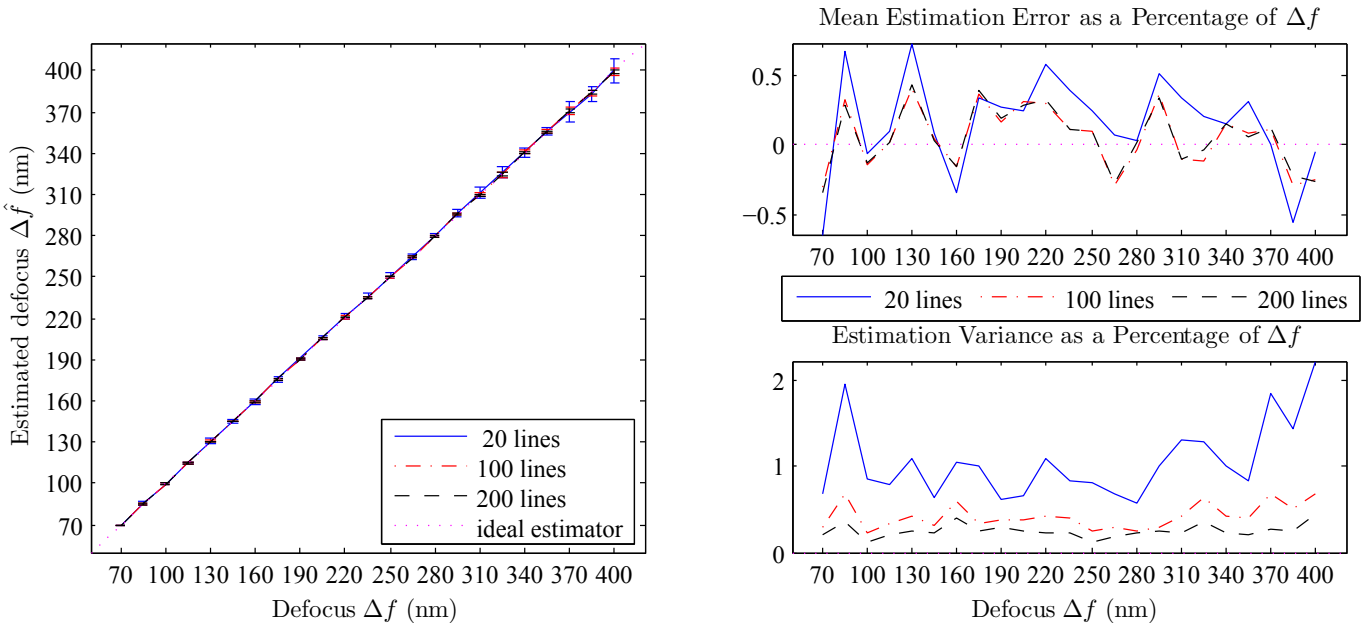

Fig. 3. Left: Mean of the defocus estimates obtained by applying POEM to groups of, respectively, 20, 100, and 200 simulated image lines created at different defocus values with $\delta = 9$ nm, $q_0 = 0.152$ nm^{-1}, and $C_s = 1$ mm. The error bars, which decrease as the number of considered image lines increases, denote a ± 1 standard deviation range around the mean defocus estimates. Right top: Mean estimation error expressed as a percentage of Δf. Right bottom: Estimation variance expressed as a percentage of Δf.

latter case, an autoregressive moving average model is first fit to the data and then used to compute the autocorrelation of $\boldsymbol{I}_\theta$ analytically. ARMASA can perform these tasks automatically [14].) It was found through simulation studies that, for POEM testing purposes, the ARMASA approach produces the better results.

Defocus Estimation: The defocus can be estimated by introducing (7), together with (2)-(4) and the inverse Hankel transform calculation, into a nonlinear function minimizer. However, given that the range of defocus values at which a STEM is operated is known beforehand, i.e., $\Delta f \in [\Delta f_{\min}, \Delta f_{\max}]$, it is computationally faster to compute

$$\Delta\hat{f} = \min_{\Delta f_i} \|\hat{\mathfrak{p}} - \mathfrak{H}^{-1}\{\mathfrak{P}^2_{\Delta f_i}\}\|^2, \tag{8}$$

where $\Delta f_i \in [\Delta f_{\min}, \Delta f_{\max}]$, $i = 1, \ldots, N$. Although this procedure is suboptimal, its accuracy can be improved by using a large enough N.

Simulation Studies: The defocus POEM was implemented in Matlab using the autocorrelation and defocus estimators explained above. The accuracy and precision of this implementation were tested using realizations of $\boldsymbol{I}_0$, $\boldsymbol{I}_{\pi/2}$, $\boldsymbol{I}_\pi$, and $\boldsymbol{I}_{3\pi/2}$ obtained from simulated bright-field images (these are the central horizontal and vertical lines in an image). The images were generated using (1)-(4) for 23 defocus values ranging from 70 nm to 400 nm. In all cases, $\boldsymbol{v}(x, y)$ was taken to be an independent identically distributed process with common uniform distribution between -1 and 1. The image size was set to 512×512 pixes (i.e., 256 pixels per radial image line), the pixel separation was 0.1 nm, $C_s = 1$ mm, $\delta = 9$ nm, and $q_0 = 0.152$ nm^{-1} (these values lie within these parameter's typical value ranges, see [5]). For every defocus value, 3 different groups of image lines were created. Each group contained 15 sets of, respectively, 20, 100 and 200 radial image lines. This data was then used to generate, via (8) (with $\Delta f_{\min} = 50$ nm, $\Delta f_{\max} = 450$ nm, and $N = 3501$), 3 groups of 15 defocus estimates. Finally, each groups' mean and standard deviation was computed an plotted. The results are shown in Figure 3.

In the left plot in this figure, the 45° dotted line represents the response of an ideal estimator (i.e., $\Delta\hat{f} = \Delta f$). The other three lines represent the mean of the 15 defocus estimates obtained by applying POEM to groups of, respectively, 20, 100, and 200 simulated image lines. The mean estimation error as a percentage of the defocus, Δf, is shown in the top right plot. The simulation results suggest that the relative size of the mean estimation error is small and largely independent of the defocus value. Moreover, the results do not suggest the presence of bias in POEM. On the other hand, the estimation variance expressed as a percentage of the defocus value is shown in the bottom right plot. This plot suggests that although the variance is relatively small, it increases with the defocus value. Thus, more radial image lines must be considered when estimating larger defocus values. Nevertheless, as is clear from this figure, increasing the number of considered image lines beyond, say, 100 lines, do not significantly increase the precision of the estimation. Also note that in these simulations, the worst estimation error (around 6%, when only 20 radial image lines are considered), is on par with that of the standard Thon ring approach (see, e.g., [2]). Moreover, this level of

accuracy was attained by using only 5120 data points, the equivalent of a 80×64 pixels images, which reduces the data acquisition time to around 102.4 ms (assuming again a pixel dwell time of 20 μs).

Finally, it was noted that the estimation precision is also affected by the objective aperture size. Smaller apertures lead to better results, since they limit the image lines' bandwidth. This, in turn, leads to less oscillating line autocorrelation functions, $\mathfrak{p}$, which can be more easily estimated from the data. Consequently, unlike the standard Thon ring approach, the defocus POEM can be applied to data acquired with the same objective aperture used for scientific image acquisition (the former require large objective apertures).

IV. Conclusions

The defocus polar rose estimation method was introduced as a new fast defocus estimation method for STEM microscopes. Initial simulation studies showed that small estimation error can be attained with significantly less data than that needed for the standard defocus estimation methods, under normal imaging conditions. More thorough simulation studies are under way and steps are being taken to validate POEM experimentally.

Acknowledgements

This research was sponsored by the CONDOR project at FEI company, under the responsibilities of the Embedded Systems Institute (ESI). CONDOR is partially supported by the Dutch Ministry of Economic Affairs under the BSIK program.

References

[1] H. Sawada, T. Sannomiya, F. Hosokawa, T. Nakamichi, T. Kaneyama, T. Tomita, Y. Kondo, T. Tanaka, Y. Oshima, Y. Tanishiro, and K. Takayanagi, "Measurement method of aberration from Ronchigram by autocorrelation function," *Ultramicroscopy*, vol. 108, no. 11, pp. 1467–1475, October 2008.

[2] A. Tejada, W. Van Den Broek, S. van der Hoeven, and A. J. den Dekker, "Towards STEM control: Modeling framework and development of a sensor for defocus control," in *Proc. 48th IEEE Conference on Decision and Control*, Shanghai, China, 2009, pp. 8310–8315.

[3] A. Tejada, A. J. den Dekker, and W. Van Den Broek, "Introducing measure-by-wire, the systematic use of control theory in transmission electron microscopy," *Ultramicroscopy*, 2011, to appear.

[4] P. Nellist, *Science of Microscopy*. Berlin Heidelberg: Springer Verlag, 2007, ch. 2.

[5] M. De Graef, *Introduction to Conventional Transmission Electron Microscopy*. Cambridge: Cambridge University Press, 2003.

[6] S. Van Aert, A. J. den Dekker, A. van den Bos, and D. Van Dyck, "High-resolution electron microscopy: From imaging toward measuring," *IEEE Trans. Instrum. Meas.*, vol. 51, no. 4, pp. 611–615, August 2002.

[7] K. W. Urban, C. Jia, L. Houben, M. Lentzen, S. Mi, and K. Tillmann, "Negative spherical aberration ultrahigh-resolution imaging in corrected transmission electron microscopy," *Philos. Transact. A Math. Phys. Eng. Sci.*, vol. 367, no. 1903, pp. 3735–3753, 2009.

[8] G. Y. Fan and J. M. Cowley, "The simulation of high resolution images of amorphous thin films," *Ultramicroscopy*, vol. 21, pp. 125–130, 87.

[9] R. N. Bracewell, *The Fourier Transforms and Its Applications, Third Edition*. McGraw-Hill, 2000.

[10] W. M. J. Coene and T. J. J. Denteneer, "Improved methods for the determination of the spherical aberration coefficient in high-resolution electron microscopy from micrographs of an amorphous object," *Ultramicroscopy*, vol. 38, no. 3-4, pp. 225–233, July 1991.

[11] M. Vulovic, B. Rieger, L. van Vliet, A. Koster, and R. Ravelli, "A toolkit for the characterization of CCD cameras for transmission electron microscopy," *Acta Crystallogr. D Biol. Crystallogr.*, vol. 66, no. 1, pp. 97–109, 2010.

[12] G. E. P. Box, G. M. Jenkins, and G. C. Reinsel, *Time Series Analysis: Forecasting and Control*. Prentice Hall, 1976.

[13] P. M. T. Broersen, "Automatic spectral analysis with time series models," *IEEE Trans. Instrum. Meas.*, vol. 51, no. 2, pp. 211–216, Apr. 2002.

[14] ——, *Automatic Autocorrelation and Spectral Analysis*. London: Springer-Verlag, 2006.

[15] ——. ARMASA toolbox for Matlab. [Online]. Available: http://www.mathworks.com/matlabcentral/fileexchange/1330